npj | 2D materials and applications

Article

Published in partnership with FCT NOVA with the support of E-MRS

https://doi.org/10.1038/s41699-025-00548-2

UV-enhanced exfoliated $MoS_2/PtSe_2$ heterostructure for ultra-sensitive NO_2 detection at room temperature

Mubdiul Islam Rizu [1,2,3], Dalal Fadil [1,2,3] ✉ & Eduard Llobet [1,2,3] ✉

We report a $MoS_2/PtSe_2$ heterostructure-based gas sensor for detecting trace levels of NO_2 gas at room temperature. Both MoS_2 and $PtSe_2$ were synthesized by mechanical exfoliation, and the heterostructure was prepared using deterministic dry transfer method. Comprehensive characterization was performed using optical microscopy, field emission scanning electron microscopy, energy-dispersive X-ray spectroscopy, high resolution transmission electron microscopy, Raman spectroscopy and atomic force microscopy. The lateral shape of the heterostructure efficiently adsorbed NO_2 molecules. The sensor exhibited limited response and recovery in dark conditions. However, under UV illumination, the sensor showed remarkable response of 2180% and 117% towards 800 ppb and 50 ppb NO_2, respectively, with complete recovery. The theoretical limit of detection was found to be 3 ppb, and the sensitivity towards NO_2 sensing was 3.217% ppb^{-1}, which is noteworthy. Furthermore, the sensor demonstrated distinct selectivity, excellent repeatability and stability. These findings are expected to significantly advance ongoing research on TMDC-based heterostructures for gas sensing application.

Since the dawn of modern civilization, air pollution caused by hazardous, toxic, flammable gases have become one of the prime intimidations for environmental sustainability[1]. According to the World Health Organization (WHO), the degradation of indoor and outdoor air quality increases the risk of chronic respiratory infections, asthma, cardiovascular disease, bronchitis, stroke, pneumonia, and lung cancer[2]. Among the toxic gases, NO_2 (nitrogen dioxide) is a greenhouse acidic gas with stinky smell produced by burning fossil fuels at high temperature and vehicular exhausts. In accordance with the Scientific Committee on Occupational Exposure Limits (SCOEL) of European Commission, the maximum 8 h of time-weighted average (TWA) exposure to NO_2 is 0.5 ppm meanwhile the short-term exposure limit (STEL) is 1 ppm of NO_2 in 15 min timeframe[3]. Moreover, over exposure of NO_2 may paralyze human respiratory system even at ppb level concentrations[4]. Therefore, it is essential to accurately detect trace level of NO_2 gas with a precise selectivity.

In the concurrent time, semiconductor based chemiresistive gas sensor has been a prospective candidate for gas sensor industries because of its simple sensing mechanism, facile fabrication process, miniaturization, low-cost and real-time gas detection technique[5]. In general, this type of sensor comprised of an insulating substrate, interdigitated electrodes, and a substrate heater. Their transduction scheme is based on the change of electrical conductivity in response to different gaseous species. In this regard, Metal oxides (MOX) based gas sensors have demonstrated their potential as sensing materials during the past few years[6]. To date, researchers have investigated various MOX with distinct morphologies including one dimensional (nanorods, nanowires, nanoribbons), two dimensional (nanoflakes, nano sheets, nanoplates) and three dimensional (nano arrays, nanoflowers) nanostructures to enhance sensing performance. Although they are inexpensive, compact in size and exhibit high sensitivity, they suffer from poor selectivity, baseline drift and long recovery time. Nevertheless, they only function properly at higher operating temperatures (200 °C–400 °C) resulting in significant energy consumption[7].

In pursuit of potential substitutes for MOX, various low-dimensional materials-based gas sensors have been explored. Conductive polymer can be used in the low temperature application having facile production capacity[8]. Highly porous carbon nanotubes (CNTs) exhibit good sensitivity with distinct gas adsorption performance[9]. However, these materials also suffer from humidity dependent adverse effect, deterioration, long recovery time and complex manufacturing processes. The invention of graphene and two-dimensional (2D) materials have opened a new door in the domain of gas sensing[10]. Owing to superior carrier mobility and large surface area, Graphene has been inspected as sensing material to a greater extent. But it's zero

[1]School of Engineering, Universitat Rovira i Virgili, MINOS, Tarragona, Spain. [2]IU-RESCAT, Research Institute in Sustainability, Climatic Change and Energy Transition, Universitat Rovira i Virgili, Vila-seca, Spain. [3]TecnATox - Centre for Environmental, Food and Toxicological Technology, Universitat Rovira i Virgili, Tarragona, Spain. ✉e-mail: dalal.fadil@urv.cat; eduard.llobet@urv.cat

bandgap and less environmental stability are the prime challenges towards practical gas sensing applications. Furthermore, the presence of any non-carbon elements can hinder the hexagonality of graphene lowering its gas sensing performance[11].

Transition metal dichalcogenides (TMDCs) have been extensively studied as potential aspirant for futuristic IoT integrable gas sensing networks. These exceptional 2D Van der Waals (vdW) materials possess unprecedented physical, chemical, and electronic properties such as superior charge-carrier mobilities, high current on/off ratios, large surface-to-volume ratio, tuneable bandgap and appropriate surface energy levels for gas adsorption[12]. A variety of TMDC based gas sensors have already demonstrated auspicious performance while operating at room temperature (RT). Among them, both MoS_2 and $PtSe_2$ have individually drawn attention for selectively NO_2 sensing. Layered MoS_2 exhibits some advantageous properties such as high carrier mobility, low effective electron mass, variety of active functional sites for developing ultra-fast gas sensor. In addition, the absence of dangling bond as well as low binding energy for creating Mo and S vacancies enable MoS_2 for fast NO_2 sensing[13]. On the other hand, the group-10 TMDC $PtSe_2$ is also considered as a promising material for gas sensing because of its intriguing layer dependent properties, large surface-to-volume ratio, air stability, high on /off ratio and so on. Moreover, the large adsorption energy and smaller relaxed height of NO_2 above Pt-Se bond clearly indicate to the superior sensing ability of $PtSe_2$ towards NO_2 trace detection[14]. Yet, the weak interaction between the surface of MoS_2 and gas molecules is still a limiting factor for achieving higher sensing response.

The possible solutions to the aforementioned challenges could be surface functionalization, defect engineering, heterostructure formation and decoration with metal nanoparticles. Among them, laterally/vertically stacked heterostructures comprising different TMDCs can achieve superior heterointerface even in the lattice-mismatched system and significantly improve the intrinsic electronic properties. These vdW heterostructures have several novel features such as, long exciton lifetime, ultrafast charge transfer, carrier recombination which facilitate and enhance the overall gas sensing performance[15]. In conjunction, UV light illumination can improve the response and recovery rate by creating additional photo generated electron-hole pairs in the active sites[16]. Recently, several MoS_2 based heterostructure gas sensors have been reported for the detection of NO_2[17–25]. To the best of our knowledge, a $MoS_2/PtSe_2$ heterostructure based gas sensor has not been reported to date.

In this study, we explored a $MoS_2/PtSe_2$ heterostructure as a gas sensor. First, we fabricated the metal electrodes on SiO_2/Si substrate and then synthesized both MoS_2 and $PtSe_2$ by mechanical exfoliation. Then, the formation of their heterostructure was carried out using dry transfer process at room temperature. The physical structure, surface morphology and chemical composition of as prepared heterostructure was examined with optical microscope, field emission scanning electron microscopy (FESEM) and energy-dispersive X-ray spectroscopy (EDX) respectively. The crystallinity of the nano flakes was verified by high resolution transmission electron microscopy (HRTEM) and corresponding selected area electron diffraction (SAED) pattern. The structural fingerprint was confirmed with Raman spectroscopy. atomic force microscopy (AFM) was used to study the surface topography and thickness of the heterostructure. The electrical properties were evaluated by measuring its I-V characteristics. We tested the sensor for NO_2 detection at room temperature with and without UV light assistance, assessing its selectivity and the impact of moisture on its performance. Finally, we proposed the gas sensing mechanism of our $MoS_2/PtSe_2$ heterostructure sensor towards NO_2 detection.

Methods

Fabrication of metal electrodes

To prepare the metal electrodes, a highly doped Si substrate covered with a 285 nm SiO_2 insulation layer was ultrasonically cleaned with acetone, isopropyl alcohol (IPA) and deionized (DI) water for ten minutes consecutively. Then, the metal electrodes (100 nm Au/10 nm Ti) were patterned by laser lithography (DWL 66 fs, Heildelberg Instruments) followed by metal deposition using RF sputtering (Orion 8HV, AJA International). Finally, we lifted-off the metal electrodes and successively cleaned them with IPA and DI water.

Material synthesis and dry transfer

The $MoS_2/PtSe_2$ heterostructure was performed by a high-yield, all-dry deterministic viscoelastic stamping top-down synthesis method[26]. Supplementary Fig. 1 shows the schematic overview of the synthesis and dry transfer process. MoS_2 and $PtSe_2$ flakes were mechanically exfoliated (ME) from their bulk crystals using scotch tape, and then transferred onto separate Polydimethylsiloxane (PDMS) films (GelPak) hold by a 4 by 4-inch glass slide. The alignment and transfer of the flakes over prepatterned electrodes on a SiO_2/Si substrate were performed using the Karl Suss MJB4 mask aligner. The glass slide was attached to the mask aligner holder while the substrate was positioned on the chuck. The target flakes were selected to fit the gap between the electrodes. First, the $PtSe_2$ flake was aligned followed by the MoS_2 flake using micromanipulators. The alignment and the transfer process were monitored under an optical microscope integrated to the mask aligner.

Structural characterization

The physical structure of the $MoS_2/PtSe_2$ heterostructure was observed using a confocal microscope (Leica DM2500 Microsystems). The surface morphology was analysed with field emission scanning electron microscope (FESEM) (Thermo Scientific, Scios 2 DualBeam) at a high vacuum mode with an electron acceleration voltage of 5 KV. The chemical composition of the active layer was examined using the energy-dispersive X-ray spectroscopy (EDX) integrated to the FESEM system. A JEOL F200 TEM ColdFEG operated at 200 kV was used for the high-resolution transmission electron microscopy (HRTEM) characterization. HRTEM images and electron diffraction patterns were acquired with a Gatan OneView camera, a CMOS-based and optical fiber-coupled detector of 4096 by 4096 pixels. Gatan Digital Micrograph program was used to process the HRTEM images. Raman spectroscopic measurements were conducted with Renishaw InVia spectrometer utilizing a long working distance objective lens with 50× magnification (0.75 numerical aperture) and 633 nm laser wavelength. These measurements had 10 s exposure time, averaging three consecutive scans. The diffraction grating was set to 1200 lines/mm, and the laser power was maintained at 0.5 mW to prevent laser heating. The thickness, roughness and surface topography of the flakes were evaluated by the atomic force microscopy (AFM) (Agilent 5500). The AFM was operated in contact mode within $59.80 \times 59.80\ \mu m^2$ scan area, with a scan speed of 0.5 line/second and 512 scanning lines. The Keysight B2902A precision source/measure unit was used to verify the electrical properties of the heterostructure.

Gas sensor formation and measurement system

The exfoliated $MoS_2/PtSe_2$ heterostructure was bonded to a printed circuit board (PCB) via platinum wire to complete the gas sensor circuit. A customized gas detection system shown in Supplementary Fig. 2 was used for all the gas sensing measurements. The sensor was placed in an airlocked, homemade Teflon chamber with an inner volume of 25 cm^3, capable of accommodating up to four sensors simultaneously. Two ultra-bright deep violet LEDs (Thorlabs, LED370E, 375 nm, 2.5 mW) were integrated with a stainless-steel frame on top of the chamber. A computer-controlled mass-flow system (EL-Flow, Bronkhorst) provided a steady flow of gases into the inlet of the chamber at a rate of 100 mL/min, while the outlet was connected to the exhaust. In addition, a controller evaporator mixer (W-202A, Bronkhorst) installed at the chamber's inlet to quantify the gas-sensing performance in humid environment. The sensor resistance variations were monitored using the Keysight Benchview Data Acquisition System (DAQ970A). For our experiments, calibrated NO_2 gas cylinder (1ppm concentration) diluted with dry air was used, and the sensor was always tested at room temperature. The sensor was periodically exposed to the NO_2 gas for 10 min, followed by 1 h under dry air to recover the baseline. The

sensor responses were calculated using the Eq. (1).

$$\%Response = \frac{R_{gas} - R_{air}}{R_{air}} \times 100 \quad (1)$$

Where R_{gas} and R_{air} denote the resistance recorded in the target analyte and dry air respectively.

Results

Morphological and topographical studies

Figure 1a shows the cross-sectional schematic diagram of the $MoS_2/PtSe_2$ heterostructure device. Our PCB-bonded prototype gas sensor, where two of the electrodes on the SiO_2/Si substrate are connected with platinum wires is displayed in Supplementary Fig. 3. Figure 1b illustrates the surface morphology from the FESEM analysis. Over the metal electrodes, a $PtSe_2$ flake and a MoS_2 flake are overlapped from bottom to top. Notably, the thin MoS_2 flake is nearly transparent, allowing visibility of the underlying small $PtSe_2$ flake and electrodes. The $PtSe_2$ flake lying under the MoS_2 flake bridges the gap between the two electrodes. The target gas adsorption occurs on the outer MoS_2 flake which is exposed to the environment. However, the charge carriers transferred between the adsorbed molecules and the gas sensitive film must travel across the $MoS_2/PtSe_2$ interface to be collected by the electrodes[27]. The dimensions of the heterostructure measure approximately $32 \times 32\ \mu m^2$, an ideal size for effective adsorption of the target gas within the sensing channel. Figure 1c shows the EDX analysis of the exfoliated $MoS_2/PtSe_2$ heterostructure formed on the SiO_2/Si substrate, indicating a strong presence of Mo, S, Pt and Se with minimal impurities. The quantitative microanalysis of the elements is shown in Supplementary Table 1 in detail. The HRTEM image of MoS_2 flake in Supplementary Fig. 4a clearly displays the single crystalline layers. The interlayer distance was found 0.27 nm corresponding to the (100) crystallographic plane of MoS_2[28]. The SAED pattern in Supplementary Fig. 4b exhibits hexagonal symmetrical patterns, indicating the hexagonal lattice structure of MoS_2 crystals. On the other hand, the HRTEM image of $PtSe_2$ flake also shows single crystalline nature as shown in Supplementary Fig. 5a. The interlayer distance around 0.186 nm ascribing to the (110) plane of $PtSe_2$ comply with the existing literature[29]. Corresponding SAED pattern in Supplementary Fig. 5b shows hexagonally arranged diffraction spots, strongly addressing its highly crystalline feature. The surface topography obtained by AFM (Fig. 1d) clearly shows the thin layers of MoS_2 and $PtSe_2$ flakes. The average roughness was 1.456 nm and the root mean square roughness was 2.018 nm, which is favorable for gas sensing by creating more active sites on the flake surface[30]. Figure 1e reveals the thickness of the heterostructure measured to be 14 nm, by exporting the corresponding height profile along the white line AB shown in Fig. 1d. The thickness of the $PtSe_2$ flake is found around 6 nm as shown in Supplementary Fig. 6. Therefore, the thickness of the MoS_2 flake is around 8 nm since the heterostructure is vertically stacked.

Raman spectrum analysis

The structural fingerprint of the $MoS_2/PtSe_2$ heterostructure, obtained by Raman spectroscopy in the 150 to 430 cm^{-1} regions, is depicted in Fig. 1f. For $PtSe_2$, the prominent peaks at 175 cm^{-1} and 205 cm^{-1} correspond to the E_g in-plane and A_{1g} out-of-plane vibrations of selenium atoms, respectively, consistent with existing literature[31]. Another less prominent longitudinal optical (LO) mode, associated with the overlapping of infrared (IR) active modes E_u and A_{2u} appears at 235 cm^{-1}. The relative intensity of this LO peak indicates the existence of very thin of $PtSe_2$ flake beneath the MoS_2 flake. The A_{1g}/E_g ratio was found to be 0.55, suggesting decreased van der Waals interactions between the layers due to the low layer number[32]. For MoS_2, the two characteristic Raman active modes, E^1_{2g} and A_{1g} are observed at 383 cm^{-1} and 407 cm^{-1} corresponding to the in-plane vibrations of Mo and S atoms and the out-of-plane vibrations of S atoms, respectively[33]. The Raman frequency difference between these two active modes is 24 cm^{-1}, suggesting a thickness of 3 or 4 layers[34]. The full width at half maximum (FWHM) for E^1_{2g} and A_{1g} were calculated as 4 cm^{-1} and 9 cm^{-1}, respectively, indicating the presence of nano-crystalline MoS_2[35]. There is another asymmetric peak at 420 cm^{-1} in addition to the typical Raman peaks for MoS_2 which can be ascribed to Mo-S vibrations for oxysulfide species[36]. During exfoliation as well as dry transfer process, atmospheric oxygen may react with Mo–S–Mo bonds at the edge of the flake, because of the existing dangling bonds[37].

Electrical properties

The I–V characteristic of the exfoliated $MoS_2/PtSe_2$ heterostructure is depicted in Fig. 1g. The current is presented in logarithmic scale with a bias voltage ranging from −5 V to +5 V at room temperature. The electrical transport characteristics of the device clearly indicate the formation of Schottky contacts between the thinner MoS_2 layer and the Au/Ti electrodes due to the difference of their work functions[38]. Moreover, the device displayed the rectifying behavior based on the Schottky barrier formed in the junction. The high forward current 5.48×10^{-7} A at +5 V and the low reverse current 4.25×10^{-8} A at −5 V having rectification ratio of 13 indicates the formation of p-n junction between the MoS_2 and $PtSe_2$ nanoflakes[39].

Gas sensing performance analysis

The gas sensing performance of our $MoS_2/PtSe_2$ heterostructure device was assessed by monitoring its relative resistance changes upon exposure to a specific concentration of NO_2. Initially, the sensor was tested towards 500 ppb NO_2 at room temperature (Fig. 2a). Upon expose to the oxidizing gas NO_2, an increase in resistance was observed, indicating n-type semiconducting behavior with electrons as the majority charge carriers. In Fig. 2a, the sensor exhibited a 13% response but did not recover after subsequent exposure to dry air, likely due to the high adsorption energy of NO_2 molecules on the heterointerface. When exposed to higher concentrations of the target gas, the sensor required a comparatively longer recovery time to desorb the molecules from its surface, especially for small nanoflakes. This led to baseline drift[40].

To accelerate the recovery time, we applied a constant UV illumination to the sensor. We observed that the baseline resistance shifted from mega to kilo Ohm range when the sensor operation was switched from dark to UV illumination, as UV light helps desorb molecules from the sensor surface. Figure 2b shows the UV-assisted dynamics of the $MoS_2/PtSe_2$ heterostructure sensor towards 500 ppb NO_2 at room temperature. With UV illumination, the baseline fully recovered, and the sensor exhibited a very high response of 1382%. The first two responses in Fig. 2b are slightly lower because the UV light initially cleans the surface when it is turned on and kept constant. In this case, NO_2 molecules capture electrons, generating NO_2^- and increasing overall sensor resistance. The photo-generated holes from the UV illumination react with this NO_2^-, form NO_2 gas, thus favouring a quick recovery of the baseline. During each recovery cycle, negligible overshoots were observed, likely due to small interruptions of the mass flow controller during concentrations change[41]. Figure 2c shows the variation of the sensor resistances upon exposure to the consecutive NO_2 concentrations ranging from 50 ppb to 800 ppb at room temperature. The resistance increased with rising NO_2 concentrations. The baseline remained stable with minimal noise levels, indicating high signal-to-noise ratio. From Fig. 2c, the sensor responses were calculated as 117%, 325%, 932%, 1673% and 2180% for 50 ppb, 100 ppb, 200 ppb, 500 ppb, and 800 ppb respectively, showing an exponential increase in response with increasing NO_2 concentrations. Repeatable cycles for all these individual NO_2 concentrations were observed, these are shown in Supplementary Fig. 7, which validate the reproducibility of our sensor.

The response time and the recovery time are two critical parameters for evaluating gas sensing performance under ambient conditions. The response time (t_{res}) and the recovery time (t_{rec}) of the sensor are defined as the time taken to reach 90% of the maximum response during gas exposure and 10% during the recovery in dry air, respectively. The calculated response

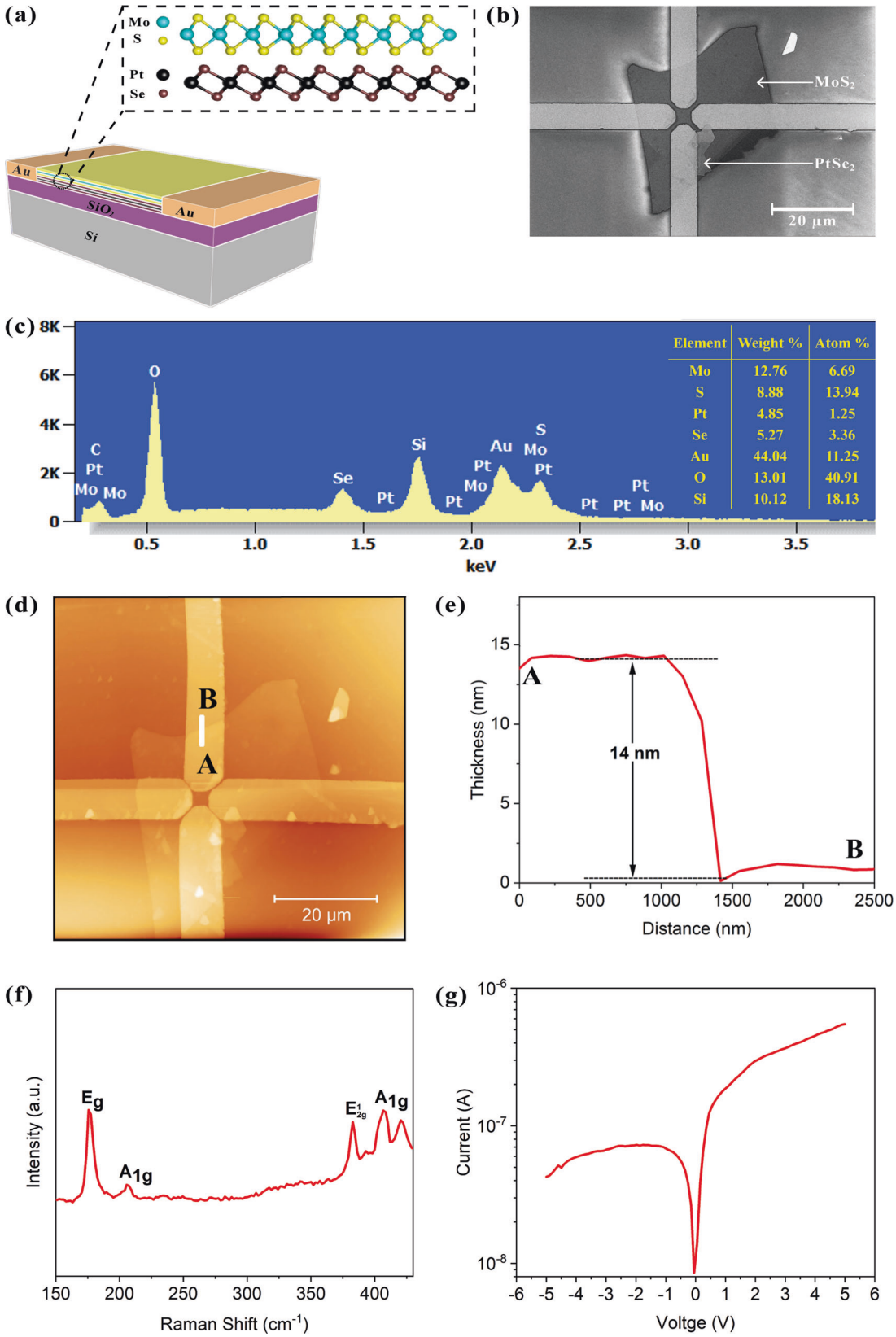

Fig. 1 | Characterization of $MoS_2/PtSe_2$ Heterostructure. a Cross-sectional schematic diagram of $MoS_2/PtSe_2$ heterostructure device. **b** FESEM image showing a small $PtSe_2$ flake compared to large MoS_2 flake. **c** EDX microanalysis highlighting the presence of Mo, S, Pt and Se atoms. In the inset FESEM image, the red marked area represents the location of EDX. **d** AFM topographical image of the sensing layer. (**e**) Corresponding height profile along the white line AB in (**d**), indicating a thickness of approximately 14 nm. (**f**) Raman spectroscopic analysis showing characteristic peaks of MoS_2 and $PtSe_2$. **g** I–V characteristics displaying the formation of asymmetric Schottky contacts, with current on logarithmic scale.

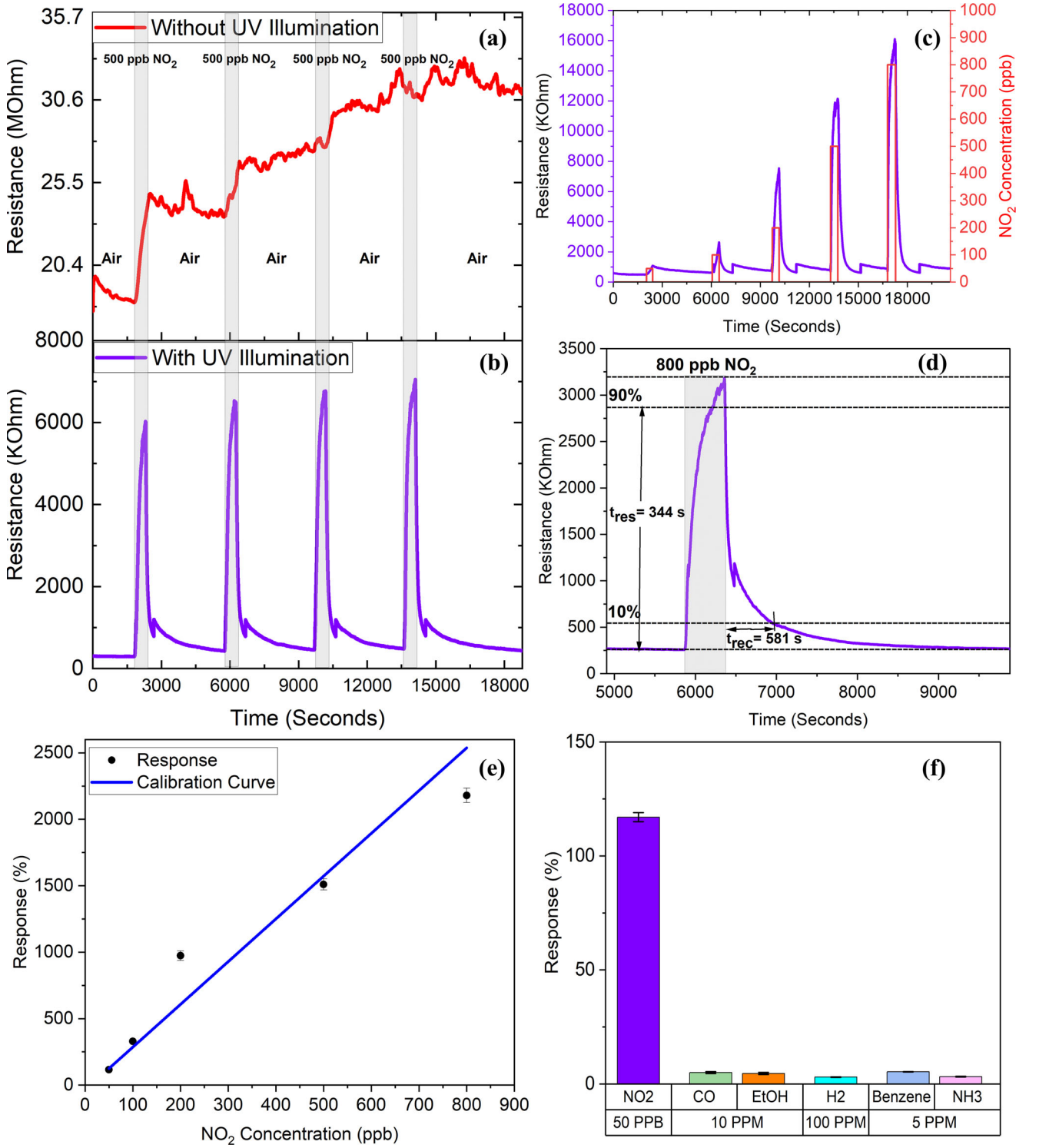

Fig. 2 | Sensing performance in dry condition. a Sensor resistance dynamics for 500 ppb NO_2 without UV illumination and (**b**) with UV illumination, (**c**) Electrical response to different NO_2 concentrations (50, 100, 200, 500 and 800 ppb) at room temperature, (**d**) Quantification of response and recovery times for 800 ppb NO_2, (**e**) Calibration curve obtained from different NO_2 concentrations, (**f**) Selectivity test results.

and recovery time for 800 ppb NO_2 are depicted in Fig. 2d. The sensor took 344 s to reach the 90% of the maximum response and the recovery time was 581 s, which is commendable compared to some existing MoS_2-based sensors[42,43]. The response and the recovery times for NO_2 concentrations ranging from 500 ppb to 50 ppb are calculated and presented in Table 1. The data indicate that response time increases while the recovery time decreases with the reduction in NO_2 concentrations, due to the diffusive capabilities of the target gas molecules.

Figure 2e shows the calibration curve drawn from the sensor responses towards NO_2 concentrations ranging from 50 ppb to 800 ppb, using a linear fit function. According to the regression analysis derived from the calibration curve, the Pearson correlation coefficient (R) and the squared correlation coefficient (R^2) were found 0.97 and 0.95 respectively, demonstrating a strong accuracy in gas sensing measurements[44]. The sensitivity (S) was determined to be 3.217% ppb^{-1} from the slope of the calibration curve. A systematic methodology in accordance with the IUPAC definition was

utilized to determine the theoretical limit of detection (LOD)[45]. The LOD is given by the Eq. (2),

$$LOD = \frac{k * s_B}{S} \quad (2)$$

Where s_B is the standard deviation of the baseline resistances, found to be 3.47, k is a numerical factor (with a recommended value is 3), and S is the Sensitivity. The calculated theoretical LOD was 3 ppb for our sensor, demonstrating its superior capability to detect very low concentrations of NO_2.

Table 1 | Response and recovery time for different NO_2 concentrations

NO_2 Concentrations (ppb)	Response time (seconds)	Recovery time (seconds)
800	344	581
500	357	430
200	476	363
100	483	345
50	511	313

To evaluate the selectivity, our sensor was exposed to several reducing gases including 10 ppm of carbon monoxide (CO), 100 ppm of hydrogen (H_2), 5 ppm of ammonia (NH_3) and volatile organic compounds (VOCs) such as 10 ppm of ethanol (C_2H_6O) and 5 ppm of benzene (C_6H_6) according to their permissible toxicity level in the atmosphere. As shown in Fig. 2f, all these gases elicited very low responses compared to 50 ppb of NO_2. Evidently, the heterostructure material exhibits low sensitivity towards these gases. The selectivity test we conducted indicates that our sensor was sensitive enough to detect traces of nitrogen dioxide and was not affected by significantly higher concentrations of other environmental pollutants. This promising result ensures reliable detection to NO_2 gas in both indoor and outdoor environments.

Ambient moisture is a crucial factor that can significantly alter the gas sensing performance, especially by affecting the sensitivity. Hence, the gas sensing behavior in humid environments was evaluated and compared with measurements under dry conditions. Figure 3a displays the resistance change in humid condition (30% RH) in response to consecutive NO_2 concentrations ranging from 100 ppb to 800 ppb. In the presence of humidity, a downward shift in baseline resistance was observed due to the concurrent chemisorption of water molecules at the heterointerface, a phenomenon also reported for the metal-oxide based gas sensors[46]. The

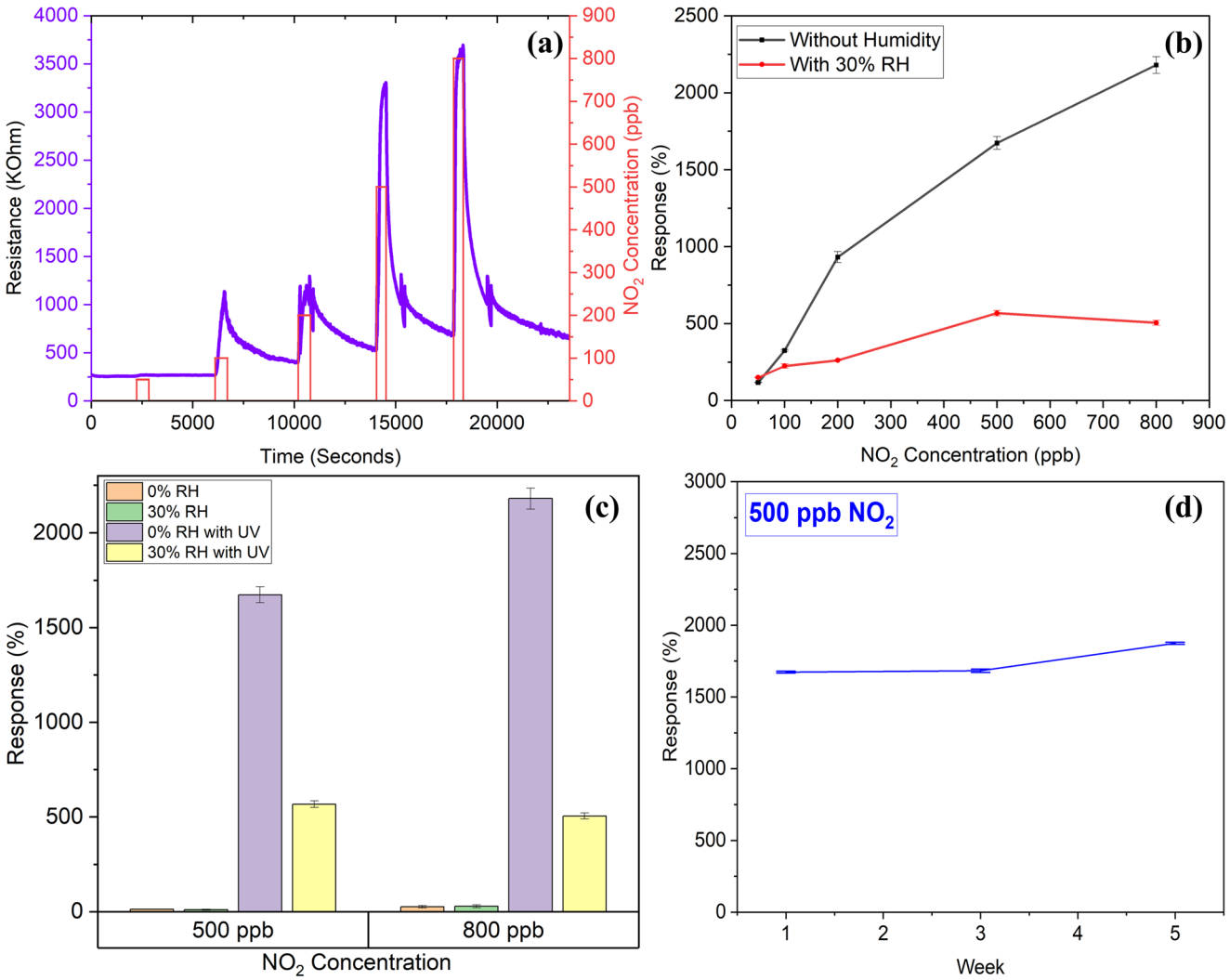

Fig. 3 | Sensing performance under humid conditions and UV excitation. a Sensor resistance dynamics for different NO_2 concentrations (100, 200, 500, and 800 ppb) at room temperature for 30% RH under UV illumination. **b** Comparison of sensor responses between ambient and 30% humid condition under UV illumination. **c** Comparison of responses with and without UV illumination for 500 ppb and 800 ppb NO_2. **d** Sensor stability for 35 days.

Table 2 | Comparison of NO_2 sensing for different MoS_2 based heterostructures

Sensing Film	Synthesis	Conc. (ppm)	T(°C)	Response (%)	Response Time (s)	Recovery Time (s)	LOD (ppb)	Refs.
Graphene/MoS_2	Hydrothermal	0.5	200	10	21.6	29.4	50	17
rGO/MoS_2	Hydrothermal	2	60	59.8	–	–	5.7	18
rGO/MoS_2/CdS	Solvothermal	0.2	75	27.4	25	34	–	19
MoS_2/MoO_3	CVD	10	RT	33.5	19	182	–	20
MoS_2/p-Si NWs	CVD	50	RT	28.4	–	–	–	21
MoS_2/ZnO NWs	CVD	50	200	31.2	–	–	200	22
Ag-Fe_2O_3/MoS_2	Solvothermal	5	120	202.2	81	355	–	23
CdTe/MoS_2	Sputtering	10	RT	40	16	114	–	24
MoS_2/SnO_2	CE	10	RT	28	408	162	500	25
MoS_2/$PtSe_2$	**ME**	**0.8**	**RT**	**2180**	**344**	**581**	**3**	**This Work**

CVD Chemical Vapor Deposition, *CE* Chemical Exfoliation, *ME* Mechanical Exfoliation.

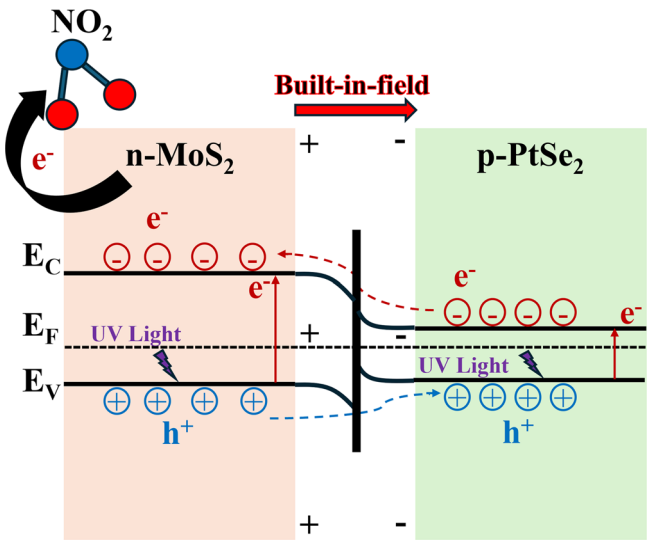

Fig. 4 | Schematic illustration of the proposed NO_2 sensing mechanism under UV illumination for the MoS_2/$PtSe_2$ heterostructure, depicted via an energy band diagram.

sensor responses were recorded as 323%, 223%, 533% and 448% for 100 ppb, 200 ppb, 500 ppb and 800 ppb of NO_2, respectively. Repeatable cycles for these NO_2 concentrations in humid conditions, are shown in Supplementary Fig. 8. However, the sensor response lacked its monotonic nature towards the increment of the NO_2 concentrations as it could not be able to discriminate between two adjacent gas concentrations. In humid condition, the adsorbed water molecules form a thin barrier-like layer hindering the interactions between the sensing layer and NO_2 molecules. This barrier significantly hampers the sensitivity leading to similar resistance reading towards changes in NO_2 concentrations[47]. Moreover, a slight drift in sensor responses was visible with the escalation of NO_2 concentrations. Comparing these results with those obtained under dry conditions (Fig. 3b), a drastic change in responses is evident. This degradation in sensor response suggests that water molecules accumulated more active sites. Water molecules acting as reducing agents, were chemisorbed within the sensing area's active sites accelerating electron removal. As humidity increased, continuous water layers formed due to physisorption, chemisorption, water molecules were ionized to H_3O^+ and transferred via the Grotthuss mechanism[48]. This proton hopping significantly decreased sensor resistance by altering its conductivity. Overall, these factors indicate that our sensor is less resilient in humid environments. To mitigate humidity interference, various anti-humidity strategies such as surface engineering, algorism compensation, parameter modulation, novel material development, and physical isolation can be implemented[49]. Figure 3c demonstrates the correlation between sensor responses under various operating conditions for NO_2 concentrations of 500 ppb and 800 ppb. Specifically, without UV illumination, the sensor exhibited a small response even in humid conditions whereas with UV illumination, a significant reduction in response was observed. Continuous deep UV light irradiation was also responsible for the deterioration of our sensor response by forming additional water droplets over the surface under the wet ambient air[50].

The sensor stability over 35 days when exposed to 500 ppb NO_2 is shown in Fig. 3d. Surprisingly, even after 5 weeks the sensor displayed a significant response due to continuous UV illumination, which enhanced the generation of active sites for NO_2 adsorption. Thus, our sensor demonstrated improved stability and reproducibility. A comparison of gas sensing performances among several existing MoS_2-based heterostructure is illustrated in Table 2. Clearly, our exfoliated MoS_2/$PtSe_2$ heterostructure gas sensor exhibits superior response towards trace levels of NO_2 gas at room temperature, although response and recovery time need to be improved.

Gas sensing mechanism

Figure 4 represents the proposed NO_2 gas sensing mechanism under UV illumination through an energy band diagram. For constructing the band diagram of MoS_2/$PtSe_2$ heterostructure, the key parameters such as band gap, work function, electron affinity, semiconducting nature for both MoS_2 and $PtSe_2$ were considered in compliance with the existing academic report[51]. Vertically stacked n-type MoS_2 and p-type $PtSe_2$ form p-n junction at the heterointerface, exhibiting n-type conductivity with electrons as the majority charge carrier. The optical energy of our UV light (375 nm) was found 3.3 eV using the Jacobian Conversion from wavelength to energy scale[52]. Exceeding the bandgaps of few layers of MoS_2 (1.2 eV)[53] and $PtSe_2$ (0.6 eV)[54], this energy excites electron-hole pairs within the heterointerface where photogenerated electrons move from the valence band to the conduction band in both materials. Due to smaller work function of $PtSe_2$ compared to MoS_2, electrons diffuse from p-type $PtSe_2$ to n-type MoS_2, while holes move in the opposite direction. When the Fermi energy levels (E_F) of the heterostructure reach equilibrium, a built-in potential and band bending occurred with the expansion of the depletion region.

In addition, the photoexcited electrons from the conduction band of $PtSe_2$ can rapidly transfer to that of MoS_2, and similarly, holes from the valence band of MoS_2 can transfer to that of $PtSe_2$. Moreover, MoS_2/$PtSe_2$ forms type-I van der Waals junction (Fig. 4), enhancing effective charge carrier separation, minimizing recombination, and consequently boosting the gas sensing capabilities[55].

Prior to NO_2 sensing, ambient oxygen molecules got adsorbed on the large MoS_2 surface during the synthesis process (Eq. 3). Upon expose to oxidizing NO_2, surface electrons are captured reducing the concentration of

majority charge carriers and increasing sensor resistance (Eq. 4). Continuous UV illumination generates the photogenerated charge carriers in both MoS_2 and $PtSe_2$ (Eq. 5). Photogenerated electrons, $e^-(h\upsilon)$ combined with adsorbed oxygen to produce $O_2^-(h\upsilon)$ (Eq. 6). $O_2^-(h\upsilon)$ and existing $e^-(h\upsilon)$ then react with adsorbed NO_2^- to form NO_2 gas, facilitating quick recovery (Eq. 7)[56].

In humid environments, the dissociative adsorption of water molecules is favored, forming surface hydroxyls[57]. This displaces the equilibrium of the adsorption of oxygen species (Eq. 6), resulting in a reduced number of adsorbed molecular oxygen under humid conditions. The reduction in the number of adsorbed molecular oxygen translates into a lower number of available surface reaction sites for nitrogen dioxide molecules (Eq. 7), which translates into a lower response.

$$O_2(ads) + e^- \rightarrow O_2^-(ads) \tag{3}$$

$$NO_2(g) + O_2^-(ads) + 2e^- \rightarrow 2NO_2^-(ads) + 2O_2^-(ads) \tag{4}$$

$$h\vartheta \rightarrow h^+(h\vartheta) + e^-(h\vartheta) \tag{5}$$

$$O_2(ads) + e^-(h\vartheta) \rightarrow O_2^-(h\vartheta) \tag{6}$$

$$NO_2^-(ads) + O_2^-(h\vartheta) + e^-(h\vartheta) \rightarrow 2O^-(ads) + NO_2(g) \tag{7}$$

Discussion

In this work, we successfully synthesized an $MoS_2/PtSe_2$ van der Waals heterostructure gas sensor for NO_2 detection using mechanical exfoliation and the dry transfer method. This top-down synthesis process favors high yield and excellent crystallinity of the materials, resulting in a superior heterointerface due to the van der Waals forces. Although baseline drift was observed during gas measurements, we developed a UV-assisted method to accelerate recovery. The sensor exhibited very high response of up to 2180% for 800 ppb at room temperature, indicating high sensitivity towards trace levels of NO_2. It also displayed exceptional selectivity compared to other reducing gases. The stability and reproducibility of the sensors were impressive over a period of 35 days. We observed a degraded response in humid environments even though there is a scope for improvement by utilizing some anti-humidity strategies in the future. For example, one approach could be combining the gas sensor with a humidity sensor while the other one would consist of coating the hybrid 2D gas-sensitive layer with an ultra-thin film able to filter out water molecules. Ultimately, our research opens new possibilities in the development of TMDC heterojunction-based gas sensors for environmental monitoring.

Data availability

The authors declare that the data supporting the finding are available within the paper and its supplementary information. The corresponding authors can also provide data upon reasonable request.

Received: 13 August 2024; Accepted: 19 March 2025;
Published online: 07 April 2025

References

1. Zivin, J. G. & Neidell, M. The impact of pollution on worker productivity. *Am. Econ. Rev.* **102**, 3652–3673 (2012).
2. Xue, Y., Wang, L., Zhang, Y., Zhao, Y. & Liu, Y. Air pollution: a culprit of lung cancer. *J. Hazard. Mater.* **434**, 128937 (2022).
3. Tato Diogo, M. European legal framework related to underground mining and tunnelling concerning commission directive (EU) 2017/164, 31 January establishing a fourth list of indicative occupational exposure limit values. *Int. J. Min. Sci. Technol.* **30**, 541–545 (2020).
4. Kampa, M. & Castanas, E. Human health effects of air pollution. *Environ. Pollut.* **151**, 362–367 (2008).
5. Tsujita, W., Yoshino, A., Ishida, H. & Moriizumi, T. Gas sensor network for air-pollution monitoring. *Sens Actuators B Chem.* **110**, 304–311 (2005).
6. Grilli, M. L. Metal oxides. *Metals* **10**, 820 (2020).
7. Tomchenko, A. A., Harmer, G. P., Marquis, B. T. & Allen, J. W. Semiconducting metal oxide sensor array for the selective detection of combustion gases. *Sens. Actuators B: Chem.* **93**, 126–134 (2003).
8. Namsheer, K. & Rout, C. S. Conducting polymers: a comprehensive review on recent advances in synthesis, properties and applications. *RSC Adv.* **11**, 5659–5697 (2021).
9. Kumar, S., Pavelyev, V., Mishra, P. & Tripathi, N. A review on chemiresistive gas sensors based on carbon nanotubes: device and technology transformation. *Sens. Actuators A: Phys.* **283**, 174–186 (2018).
10. Shi, Y., Ni, L., Wang, Z., Chen, M. & Feng, L. Ultrathin two-dimensional materials: new opportunities and challenges in ultra-sensitive gas sensing. *Coord. Chem. Rev.* **505**, 215691 (2024).
11. Tian, W., Li, W., Yu, W. & Liu, X. A review on lattice defects in graphene: types generation effects and regulation. *Micromachines* **8**, 163 (2017).
12. Llobet, E. Transition metal dichalcogenide based toxic gas sensing. *Curr. Opin. Environ. Sci. Health* **37**, 100533 (2024).
13. Zhang, S. et al. Morphological evolution of vertically standing molybdenum disulfide nanosheets by chemical vapor deposition. *Materials* **11**, 631 (2018).
14. Sajjad, M., Montes, E., Singh, N. & Schwingenschlögl, U. Superior gas sensing properties of monolayer $PtSe_2$. *Adv. Mater. Interfaces* **4**, 5 (2017).
15. Joseph, S. et al. A review of the synthesis, properties, and applications of 2D transition metal dichalcogenides and their heterostructures. *Mater. Chem. Phys.* **297**, 127332 (2023).
16. Zhou, Y., Zou, C., Lin, X. & Guo, Y. UV light activated NO_2 gas sensing based on Au nanoparticles decorated few-layer MoS_2 thin film at room temperature. *Appl Phys. Lett.* **113**, 8 (2018).
17. Long, H. et al. High surface area MoS_2/Graphene hybrid aerogel for ultrasensitive NO_2 detection. *Adv. Funct. Mater.* **26**, 5158–5165 (2016).
18. Zhou, Y., Liu, G., Zhu, X. & Guo, Y. Ultrasensitive NO_2 gas sensing based on rGO/MoS_2 nanocomposite film at low temperature. *Sens Actuators B Chem.* **251**, 280–290 (2017).
19. Shao, S. et al. A novel RGO-MoS_2-CdS nanocomposite film for application in the ultrasensitive NO_2 detection. *J. Alloy. Compd.* **774**, 1–10 (2019).
20. Kumar, R. et al. Growth of MoS_2–MoO_3 hybrid microflowers via controlled vapor transport process for efficient gas sensing at room temperature. *Adv. Mater. Interfaces* **5**, 1800071 (2018).
21. Zhao, S. et al. Highly enhanced response of MoS_2/porous silicon nanowire heterojunctions to NO2 at room temperature. *RSC Adv.* **8**, 11070–11077 (2018).
22. Zhao, S. et al. Vertically aligned MoS_2 /ZnO nanowires nanostructures with highly enhanced NO_2 sensing activities. *Appl Surf. Sci.* **456**, 808–816 (2018).
23. Yin, M. et al. Ag nanoparticles-modified Fe_2O_3@MoS_2 core-shell micro/nanocomposites for high-performance NO_2 gas detection at low temperature. *J. Alloy. Compd.* **829**, 154471 (2020).
24. Jaiswal, J., Sanger, A., Tiwari, P. & Chandra, R. MoS_2 hybrid heterostructure thin film decorated with CdTe quantum dots for room temperature NO_2 gas sensor. *Sens Actuators B Chem.* **305**, 127437 (2020).
25. Cui, S., Wen, Z., Huang, X., Chang, J. & Chen, J. Stabilizing MoS_2 nanosheets through SnO_2 nanocrystal decoration for high-performance gas sensing in air. *Small* **11**, 2305–2313 (2015).
26. Castellanos-Gomez, A. et al. Deterministic transfer of two-dimensional materials by all-dry viscoelastic stamping. *2D Mater.* **1**, 011002 (2014).
27. Deokar, G. et al. MoS_2–Carbon nanotube hybrid material growth and gas sensing. *Adv. Mater. Interfaces* **4**, 1700801 (2017).
28. Li, W. et al. Gas sensors based on mechanically exfoliated MoS_2 nanosheets for room-temperature NO_2 Detection. *Sensors* **19**, 2123 (2019).

29. Jiang, W. et al. Large-area high quality $PtSe_2$ thin film with versatile polarity. *InfoMat* **1**, 260–267 (2019).
30. Khudadad, A. I., Yousif, A. A. & Abed, H. R. Effect of heat treatment on WO_3 nanostructures based NO_2 gas sensor low-cost device. *Mater. Chem. Phys.* **269**, 124731 (2021).
31. Szydłowska, B. M. et al. Spectroscopic thickness and quality metrics for $PtSe_2$ layers produced by top-down and bottom-up techniques. *2D Mater.* **7**, 045027 (2020).
32. O'Brien, M. et al. Raman characterization of platinum diselenide thin films. *2D Mater.* **3**, 021004 (2016).
33. Chakraborty, B., Matte, H. S. S. R., Sood, A. K. & Rao, C. N. R. Layer-dependent resonant Raman scattering of a few layer MoS_2. *J. Raman Spectrosc.* **44**, 92–96 (2013).
34. Chang, C. et al. Growth of large-area and highly crystalline MoS_2 thin layers on insulating substrates. *Nano Lett.* **2**, 1538–1544 (2012).
35. Deokar, G., Vignaud, D., Arenal, R., Louette, P. & Colomer, J. F. Synthesis and characterization of MoS_2 nanosheets. *Nanotechnology* **27**, 075604 (2016).
36. Schrader, G. L. & Cheng, C. P. In situ laser raman spectroscopy of the sulfiding of Mo γ-Al_2O_3 catalysts. *J. Catal.* **80**, 369–385 (1983).
37. Payen, E., Kasztelan, S., Houssenbay, S., Szymanski, R. & Grimblot, J. Genesis and characterization by laser Raman spectroscopy and high-resolution electron microscopy of supported MoS_2 crystallites. *J. Phys. Chem.* **93**, 6501–6506 (1989).
38. Gui, T. et al. In-situ fabrication of $PtSe_2$/MoS_2 van der Waals heterojunction for self-powered and broadband photodetector. *Mater. Des.* **238**, 112722 (2024).
39. Gan, W. et al. Van der Waals heterostructure gas sensors based on narrow-wide bandgap semiconductors for superior sensitivity. *Nanotechnology* **35**, 05LT03 (2024).
40. Ricciardella, F. et al. Calibration of nonstationary gas sensors based on two-dimensional materials. *ACS Omega* **5**, 5959–5963 (2020).
41. Honeycutt, W. T., Ley, M. T. & Materer, N. F. Precision and limits of detection for selected commercially available, low-cost carbon dioxide and methane gas sensors. *Sensors* **19**, 3157 (2019).
42. Bharathi, P. et al. Conductometric NO_2 gas sensor based on Co-incorporated MoS_2 nanosheets for room temperature applications. *Sens Actuators B Chem.* **360**, 131600 (2022).
43. Fadil, D., Sharma, J., Rizu, M. I. & Llobet, E. Direct or indirect sonication in ecofriendly MoS_2 dispersion for NO_2 and NH_3 gas-sensing applications. *ACS Omega* **9**, 25297–25308 (2024).
44. Brown, A. S. et al. Analysis of natural gas by gas chromatography: Reduction of correlated uncertainties by normalisation. *J. Chromatogr. A* **1040**, 215–225 (2004).
45. Analytical Methods Committee. Recommendations for the definition, estimation and use of the detection limit. *Analyst* **112**, 199–204 (1987).
46. Bârsan, N. & Weimar, U. Understanding the fundamental principles of metal oxide based gas sensors; the example of CO sensing with SnO_2 sensors in the presence of humidity. *J. Phys. Condens. Matter* **15**, R813 (2003).
47. Pereira, N. M. et al. Aerosol-printed MoS_2 ink as a high sensitivity humidity sensor. *ACS Omega* **7**, 9388–9396 (2022).
48. Zhang, D., Tong, J. & Xia, B. Humidity-sensing properties of chemically reduced graphene oxide/polymer nanocomposite film sensor based on layer-by-layer nano self-assembly. *Sens Actuators B Chem.* **197**, 66–72 (2014).
49. Wang, Y. & Zhou, Y. Recent progress on anti-humidity strategies of chemiresistive gas sensors. *Materials* **15**, 8728 (2022).
50. Yoshihara, K., Takatori, Y., Miyazaki, K. & Kajii, Y. Ultraviolet light-induced water-droplet formation from wet ambient air. *Proc. Jpn Acad. Ser. B Phys. Biol. Sci.* **83**, 320–325 (2007).
51. Wang, W. et al. Investigation of the band alignment at MoS_2/$PtSe_2$ heterojunctions. *Appl Phys. Lett.* **114**, 20 (2019).
52. Mooney, J. & Kambhampati, P. Get the basics right: Jacobian conversion of wavelength and energy scales for quantitative analysis of emission spectra. *J. Phys. Chem. Lett.* **4**, 3316–3318 (2013).
53. Ganatra, R. & Zhang, Q. Few-layer MoS_2: a promising layered semiconductor. *ACS Nano* **8**, 4074–4099 (2014).
54. Pribusová Slušná, L. et al. Optical characterization of few-layer $PtSe_2$ nanosheet films. *ACS Omega* **6**, 35398–35403 (2021).
55. Besse, R., Wang, H., West, D., Da Silva, J. L. F. & Zhang, S. Prediction of effective photoelectron and hole separation in type-I MoS_2/$PtSe_2$ van der Waals junction. *J. Phys. Chem. Lett.* **13**, 6407–6411 (2022).
56. Zhou, Y., Gao, C. & Guo, Y. UV assisted ultrasensitive trace NO_2 gas sensing based on few-layer MoS_2 nanosheet-ZnO nanowire heterojunctions at room temperature. *J. Mater. Chem. A Mater.* **6**, 10286–10296 (2018).
57. Kumar, S. et al. A review on 2D transition metal di-chalcogenides and metal oxide nanostructures based NO_2 gas sensors. *Mater. Sci. Semiconductor Process.* **107**, 104865 (2020).

Acknowledgements

This project has received funding from the European Union's Horizon 2020 research and innovation program under the Marie Skłodowska-Curie grant agreement No. 945413, No. 101025770 and from the Universitat Rovira i Virgili (URV). Funded partially by MICINN and FEDER under grant no. PID2022-142451OB-C21. We also thank the Universitat Politècnica de Catalunya (UPC) for using their mask aligner and Dr. Gemma Lopez at UPC for her guidance in the cleanroom. E.L. is supported by the Catalan Institution for Research and Advanced Studies via the 2023 Editon of the ICREA Academia Award.

Author contributions

M.I.R. wrote the paper and designed the experiments. D.F. made the device. M.I.R. performed all the characterizations and gas sensing measurements. M.I.R. analyzed the data. E.L. and D.F. supervised the research. All authors contributed to the review, editing, and improvement of the manuscript.

Competing interests

The authors declare no competing interests.

Additional information

Supplementary information The online version contains supplementary material available at https://doi.org/10.1038/s41699-025-00548-2.

Correspondence and requests for materials should be addressed to Dalal Fadil or Eduard Llobet.